Exp Fluids (2015) 56:1
DOI 10.1007/s00348-014-1876-4

RESEARCH ARTICLE

Experimental investigation on interactions among fluid and rod-like particles in a turbulent pipe jet by means of particle image velocimetry

Alessandro Capone · Giovanni Paolo Romano · Alfredo Soldati

Received: 25 July 2014 / Revised: 8 October 2014 / Accepted: 4 December 2014 / Published online: 30 December 2014

Abstract The near field of a turbulent circular pipe jet laden with rigid rod-like particles is investigated experimentally by means of particle image velocimetry. Two mass fraction loadings are examined at a Reynolds number equal to 9,000. A simple and robust phase discrimination scheme based on image intensity threshold is presented and validated. Simultaneous flow and dispersed phase velocities data are discussed and compared to literature data for spherical and elongated particles providing insight on phase interactions. Being the Stokes number around unity, both inertial and dynamical effects have high relevance, the former giving rise to velocity lag among particles and fluid and the latter to turbulence modulation in the carrier flow induced by the dispersed phase.

1 Introduction

Understanding two-phase turbulent flows with a solid phase dispersed into a carrier fluid is of great importance in many industrial applications such as cyclone separators, post-combustor devices and chemical reactors.

Many efforts have been given in this direction, and the majority of investigations focus on two main aspects: the dispersed phase distribution and concentration induced by the flow and the modification of the fluid phase due to the presence of the solid. The former is of particular interest for industrial applications, where particle concentration within the flow represents a key factor, such as combustion devices (Longmire and Eaton 1992). On the other hand, turbulent modulation induced by the dispersed phase in the flow, which represents the focus of the current study, in addition to industrial applications, has also interest in turbulence fundamentals. This topic has been the subject of several works (Parthasarathy and Faeth 1990; Kussin and Sommerfeld 2002; Paris and Eaton 2001 among others), and a comprehensive review is given in Balachandar and Eaton (2010).

Gore and Crowe (1989) proposed a single parameter to characterize the dispersed phase effects on the turbulence intensity of the fluid phase. This parameter is the ratio d/L of the solid phase average diameter, d, to the characteristic eddy length scale L of the fluid phase. For $d/L > 0.1$, the turbulence intensity is supposed to be enhanced by the solid phase, whereas for $d/L < 0.1$, a decrease is expected (Gore and Crowe 1989). The motivation is that the drag force on particles whose diameter is smaller than the most energetic eddies dampens the turbulence intensity, whereas bigger particles produce wakes which can increase turbulence.

A historically important class of turbulent two-phase flows is represented by jets, which can be also found in several areas of engineering involving mixing, combustion and exhausting devices and represent a baseline case and a starting point for approaching more complex flows. Even for such a flow field, many works have been developed focusing on turbulence modification induced by solid particles. Fleckhaus et al. (1987) and Prevost et al. (1996) investigated experimentally the effect of particles dispersed in a gaseous jet finding that turbulence attenuation increases with particles size, in particular in the far field.

Mergheni et al. (2009) and Sadr and Klewicki (2005) focused on coaxial jets, and they compared the results to

A. Capone (✉) · G. P. Romano
Dipartimento Ingegneria Meccanica e Aerospaziale, Università La Sapienza, Rome, Italy
e-mail: alessandro.capone@uniud.it

A. Soldati
Dipartimento Ingegneria Elettrica, Gestionale e Meccanica, Università degli Studi di Udine, Udine, Italy

those predicted by the Gore and Crowe (1989) d/L criterion and found that in agreement with them for $d/L = 0.2$, an increase in dissipation and a slight enhancement of turbulence intensity is attained. Water jets laden with glass beads were investigated by Parthasarathy and Chan (2001) who found that in the far field ($x/D = 60$) particles do not affect mean velocities and normal stresses.

As a matter of fact, all these investigations used spherical particles as dispersed phase. On the other hand, in many applications, the dispersed phase cannot be deemed as spherical (pulp production, paper manufacturing, cloud formation). Rod-like particles, characterized by high (>5) geometrical aspect ratio, provide a much better approximation of the actual dispersed phase (i.e., wood fibers or ice crystals). The dynamics of rod-like fibers in shear flows have been theoretically predicted by Jeffery (1922). Such particles tend to align mostly with the mean flow although they undergo a periodic revolving motion tracing the so-called Jeffery orbits. However, it is still not clear whether in turbulent flows and specifically in turbulent jets, fibers really follow Jeffery orbits or display other motion and alignments. These features make the study of turbulence modulation effects in fiber-laden flows as compared to spherical particles particularly significant. Indeed, although some experimental and numerical works already focus on fiber suspensions in turbulent flows (Krochak et al. 2008; Parsa et al. 2011; Marchioli et al. 2010 among others), still there are few experimental studies on the effects of rod-like, fiber particles in jet flows (see Lin et al. 2012 for a numerical work on this subject). Therefore, this work aims to improve the actual knowledge on the physical phenomena involved in this specific flow and compare turbulence modulation effects by elongated particles to spherical ones. At the same time, it provides new experimental data which are necessary to tune numerical modeling.

A fiber-laden fully developed turbulent pipe jet flow is investigated by means of particle image velocimetry (PIV). The jet flow is seeded with rod-like, high aspect ratio fibers in order to investigate the modification of the fluid phase induced by the dispersed phase in the near-field region of the jet ($x/D < 5$, where D is the pipe outlet diameter). The interaction between fluid and fibers is also investigated by simultaneous analysis of particles and fluid velocity data.

In order to attain an effective separation among phases, a non-trivial image pre-processing phase is required. In the framework of optical imaging of multiphase flows, phase separation hereafter refers to the process of identification and separation of different objects within the same image. In particular, the investigation of fiber suspensions flows and in general of multiphase flows where the dispersed phase is characterized by high aspect ratios can rely upon feature detection algorithms, provided that a sufficiently high resolution is achieved (Parsa et al. 2011; Dearing et al. 2013). This approach is nonetheless time-consuming and poses significant difficulties when optical access is an issue. To this aim, in this work, we propose a robust algorithm which can be applied in general to all the cases where the dispersed fibers appear as almost spherical in acquired images. The phase discrimination method here proposed is an extension of that developed by Kiger and Pan (2000), in order to make it suitable to the present experimental conditions characterized by a narrow dimensional gap between fiber and tracer images.

In Sect. 3, the proposed phase discrimination technique is described in detail and validated by means of artificially generated images. In Sect. 4, results on the fluid phase velocity field are presented and discussed along with dispersed phase velocity data.

2 Experimental setup

The water jet apparatus shown in Fig. 1 consists of a long, horizontal, circular-section steel pipe, absolute roughness $\varepsilon = 0.015$ mm, with diameter $D = 2.2$ cm. The pipe is about $100D$ long, to establish fully developed turbulent flow conditions and extends nearly 7 cm inside the observation tank. The latter is approximately $40D$ high and wide, $80D$ long and is made of glass for full optical access. This work focuses on the near-field region of the jet where the cross-sectional area of the jet flow, estimated as three times the jet half width $R1/2$, is below $2D$ and then small compared to the observation tank size (Cater and Soria 2002). The flow is driven by a constant head tank supplied by a pump. The direction of gravity is given by the y-axis.

A high-speed PIV system is set up by means of a 8-bit BW, Photron APX CMOS camera with 1,024 × 1,024 pixels resolution at 500 Hz frame rate. The camera objective

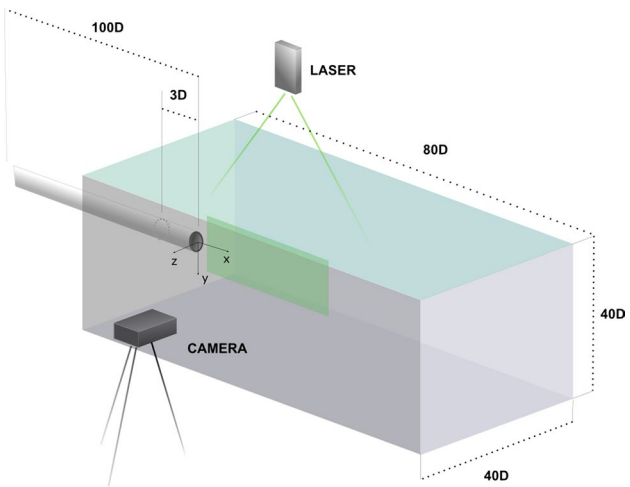

Fig. 1 Experimental setup

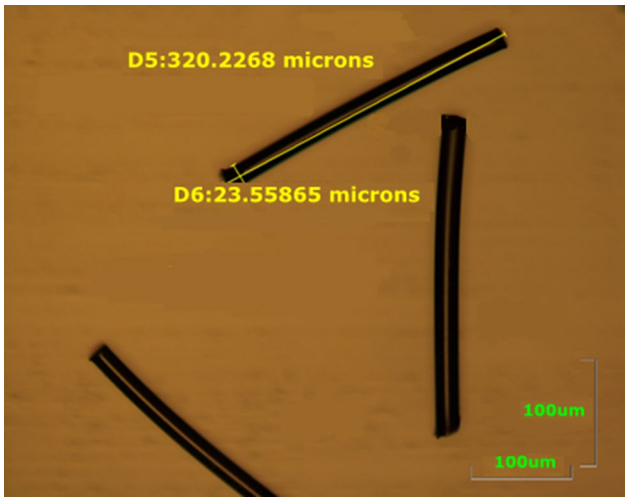

Fig. 2 Fibers microscopic image: diameter and length of a sample fiber are given (labeled in figure as D6 and D5, respectively)

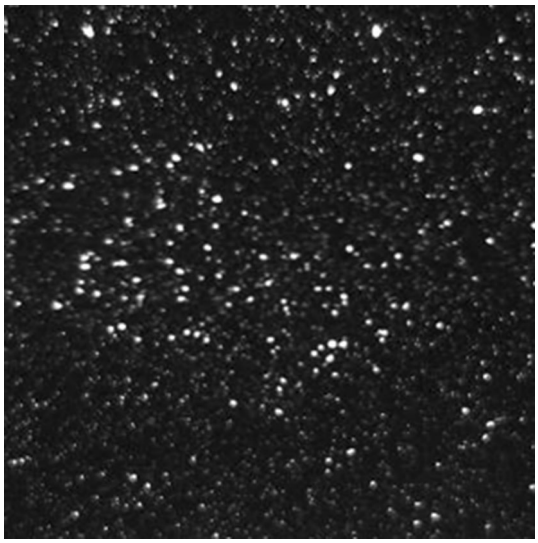

Fig. 3 Sample area of a fiber-laden flow image $C = C_2$ where both seeding particles and fibers are visible

used for all the acquisitions is a Nikon F 50-mm focal length with maximum aperture of 1.2. Lighting is provided by a continuous Spectra Physics Ar-ion laser, 488–514 nm in wavelength, with a maximum power equal to 7 W. Fluid is seeded with neutrally buoyant 10-μm-diameter hollow glass spheres (Dantec HGS-10), whereas the dispersed phase is given by nylon fibers (polyamide 6.6, density 1.13–1.15 g/cm^3, produced by Swissflock AG) with a mean length of approximately $l = 320$ μm and mean diameter 24 μm. Preliminary high-resolution acquisitions confirm that fibers do not show any bending or curling, so that they may be considered as rigid. A sample microscopic image of fibers is shown in Fig. 2 where measured diameter and length are highlighted. Acquisitions were carried out in a plane aligned with the pipe axis and covered an area of approximately 5.5D, resulting in a spatial resolution of 0.12 mm/pixel corresponding to 0.006D.

The laser sheet thickness was set approximately to 1 mm. A commercial PIV software, DaVis by LaVision Gmbh, has been employed for instantaneous fluid and dispersed phase velocity field computation. The software features an advanced image deformation multipass PIV cross-correlation algorithm with window offset, adaptive window deformation and Gaussian sub-pixel approximation thoroughly described in Stanislas et al. (2008) and a hybrid PIV/PTV algorithm for fiber tracking. The latter is based on an initial standard PIV evaluation to determine a preliminary velocity field that is used to get a robust estimator of the local velocity field. The pairing of the particles between frames is obtained from PIV displacement field by interpolation of a vector centered on the predicted particle position as described in Scarano and Riethmuller (2000). For PIV computations, minimum window size and overlap were, respectively, 32 × 32 and 75 %, leading to a vector spacing of eight pixels corresponding to approximately 0.045D. Particle tracking velocimetry (PTV) data were interpolated on a square grid of 16 pixels.

In the experiments, the jet Reynolds number based on the jet bulk velocity U_0 was 9,000, whereas Reynolds number effects have been already investigated elsewhere (Capone et al. 2013). The experimental campaign consisted in an acquisition on the single-phase jet and two on fiber-laden jet featuring two mass fractions, namely $C_1 = 0.002$ % and $C_2 = 0.006$ % (volume fraction, respectively, 0.0017 and 0.0052 %). These values were obtained by injecting a given weighted mass of fibers into the fluid volume. Laden fluid is stirred in a pre-mixing tank in order to obtain a homogeneous fiber distribution in the flow. The accuracy of concentration values is in the order of 1 %. For the present experimental conditions, $nl^3 \ll 1$ holds, where n is the number density of fibers, so that fiber suspension can be considered as dilute.

Figure 3 shows a sample of a fiber-laden image for the highest concentration case. Four sets of 4,000 images were collected in each test in order to avoid data correlation issues arising in high-speed PIV systems (Falchi and Romano 2009) and to achieve reliable statistics.

3 Phase discrimination

3.1 Algorithm description

Simultaneous velocity computation of dispersed and carrier phase in turbulent flows requires a phase discrimination step

to enable the separate application of PIV and PTV on the resulting tracer and dispersed phase images, respectively.

Phase discrimination methods may be divided in two broad categories depending on the stage when the actual discrimination is carried out (see Cheng et al. 2010; Khalitov and Longmire 2002 for a comprehensive review of both methodologies), i.e., during image acquisition (the so-called optical methods) or after image acquisition (image post-processing).

The latter has the advantage of a rather simplified experimental setup, generally requiring a single acquisition camera. As a drawback, since both phases are acquired on the same image, cross-talk error arises due to the simultaneous imaging of both phases. An example of a sophisticated, single camera-based phase discrimination scheme is thoroughly described in Bröder and Sommerfeld (2007) where a bubbly flow is investigated by means of a combination of shadow imaging, PIV and PTV. Bubbles size and orientation are identified based on a spline fitting and upon application of a median filter and a gradient-enhancing filter for edge detection.

In this work, a simple methodology for phase discrimination is proposed based on the work by Kiger and Pan (2000). A validation by means of artificial images is provided in order to assess errors in computing velocity fields. In Kiger and Pan (2000), a median filter is used to smooth out small particle images in raw pictures. Seeding-only images are obtained by subtracting the median filtered images from the original two-phase ones. The filter convolves a square two-dimensional filter stencil, $Nf \times Nf$ pixels, over the whole image. The filter width f is taken as the window size, i.e., equal to Nf. For each window position, the filter sorts the gray level values into ascending order and then selects the median value to replace the local intensity value. A thorough discussion of the optimal size f of the square median filter is also provided. If tracer and dispersed particles image size were indicated, respectively, as dt and dp, the optimal value was found to be $f/dt = 2$ for $dp/dt < 3$ and $f/dt = 1.3$ for $dp/dt \geq 3$. In the current work, due to the relatively large region imaged on the camera, the spatial resolution is not sufficient to separate fibers from fluid tracers based on their image shape. The former appear as nearly circular spots only slightly larger than tracer particle images, with $d_p/d_t \approx 2$, as shown in Fig. 3. Furthermore, fiber orientation even if not identified still affects the actual image size within the pictures. This in turn alters fibers image size distribution to the extent that the average fiber image area ranges from 3 to 10 times the average seeding tracer area. Therefore, the proposed algorithm may be successfully employed in experimental conditions where featuring a similar distribution of the dispersed phase size. The modified procedure described is required because a straightforward application of the median filter, as reported by Kiger and Pan (2000), only attenuates the tracer images without completely removing them, so that they remain still visible in the background.

Indeed, due to the narrow size gap between fiber and tracer, even the use of a broader filter, while eliminating more effectively the tracer images, simultaneously affects undesirably the fiber image quality, smearing out their borders, worsening their contrast against the background and finally making their detection more difficult.

Therefore, in order to solve this discrimination problem, a further step is applied after median filtering, i.e., a threshold on pixel intensity to identify whether a pixel belongs to a fiber or not. To avoid using arbitrary values for such intensity threshold, the choice is based on the analysis of the statistical distribution of pixel intensity within images.

Probability density functions (PDFs) of pixel intensity were computed from a set of 200 uncorrelated images. Such PDFs are fairly independent on sample number, converging within ± 10 % of the final value yet after 100 samples. Figure 4 shows the PDF obtained for single-phase and fiber-laden case at the highest concentration C_2 before and after median filter step. The probability $P(i)$ that a given pixel features an intensity value higher than a given value i is thus given by the integral of the PDF curve from i until the upper range, i.e., 255.

The results show that in comparison with the unladen case, the resulting PDF is considerably altered when fibers are present, since larger particles feature higher intensity levels and, due to their size, are less affected by the median filter. To characterize the mutual relation of the PDF curves, for each intensity value i, the probability $Pf(i)$ of a pixel having an intensity value higher than i has been calculated at first in the fiber-laden case. Then, the same has been carried out for the single-phase case $Ps(i)$ and the resulting ratio $Pf(i)/Ps(i)$ is given in Fig. 5. It may be noticed that the ratio of probabilities features an initial stage of constant slope growth followed by a plateau stage. This observation leads to the choice of the threshold value T_{int} approximately in the middle of this gradual growth region, resulting in a value in the interval 60–100, i.e., just before the plateau. The analysis of the variation of the PIV/PTV results as a function of the threshold T_{int} is the object of Sect. 3.2. The results there obtained will provide a rationale for the threshold setup in a general case. Once the value T_{int} is set, image pixels whose intensity exceeds the threshold T_{int} are labeled as pixels belonging to a fiber image. This criterion is applied to the whole image, thus obtaining a fiber-only image which can be subtracted from the original one to retrieve seeding-only pictures. The entire process is schematically summarized in Fig. 6.

3.2 Threshold setting

Post-processing discrimination methods in PIV/PTV systems introduce a source of error in PIV calculations of carrier phase due to the empty areas left in the seeding image

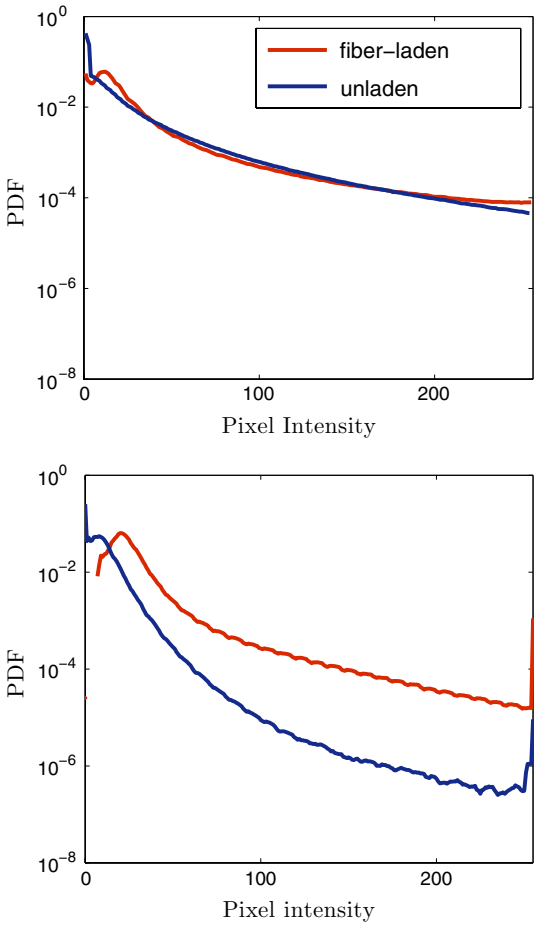

Fig. 4 PDF of light intensity at each pixel for single-phase data, compared to fiber-laden case before (at the *top*) and after (at the *bottom*) median filter

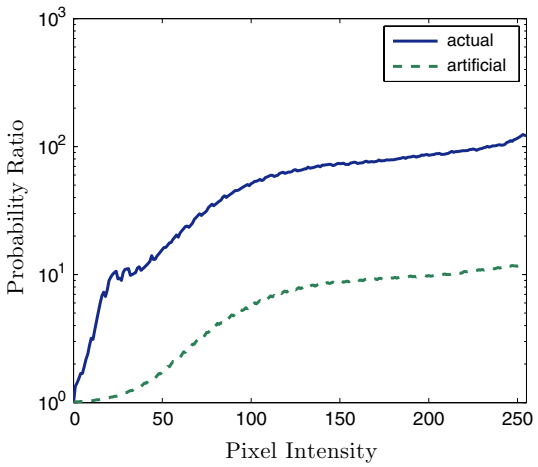

Fig. 5 Probability ratio of a pixel featuring an intensity level brighter than a certain value. Artificial data are discussed in Sect. 3.1

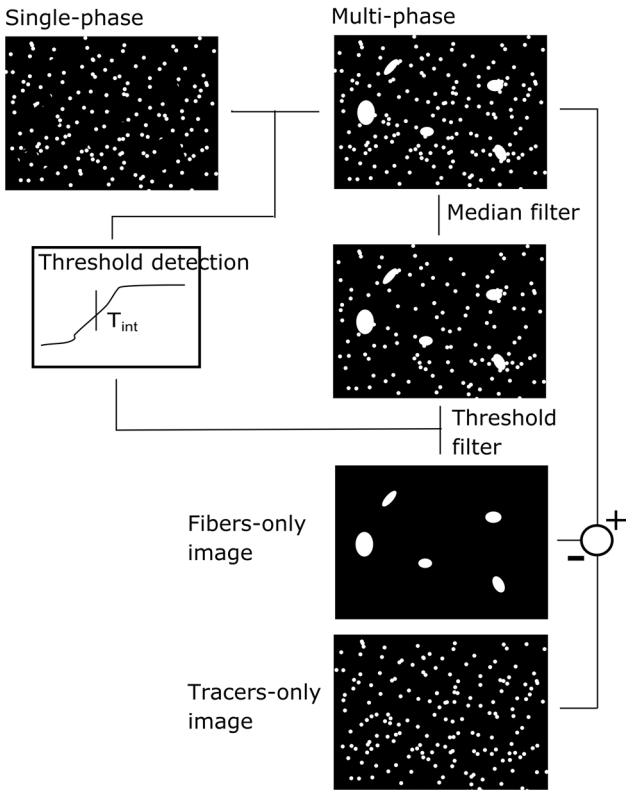

Fig. 6 Schematic of the phase discrimination algorithm

after fiber image removal (Khalitov and Longmire 2002; Kiger and Pan 2000) and in PTV results for erroneous identification of dispersed particles (particles missed or false positives).

In this section, a validation procedure to assess the magnitude of these uncertainties and their sensitivity toward T_{int} variations is outlined, in order to devise a general strategy for its optimal determination in similar experimental conditions. To this aim, in addition to single phase and to fluid and fiber, a further acquisition with fibers and no fluid tracers was performed. The results obtained are compared to PDF findings of previous section. The procedure follows that detailed in Khalitov and Longmire (2002) and Kiger and Pan (2000):

1. Seeding-only image pairs are processed, by using the commercial PIV software reported in Sect. 2, while fiber-only images are also processed to derive the fiber locations by means of a simple object detection strategy (Haralick and Shapiro 1992).
2. Artificial multiphase (seeding and fibers) images are generated by combining the fiber-only pictures with the seeding-only images of step 1.

3. The phase discrimination algorithm detailed in previous section is applied to the resulting artificial images.
4. The tracer and fiber images obtained after phase discrimination are processed separately and simultaneously to derive fluid velocity and fibers position and velocity.
5. Velocity fields obtained in step 4 are compared to those calculated in step 1, in order to assess the error induced in the phase discrimination stage. Similarly, the locations of the identified fibers in step 4 are compared to those known from step 1. This procedure is repeated for several values of T_{int}, and results are compared.

Errors in fluid velocity calculation (Kiger and Pan 2000) take the following form

$$u_{\text{err}} = \frac{1}{NM}\sum_{i=1}^{N}\sum_{j=1}^{M}\left|u_{\text{com}(i,j)} - u_{\text{ori}(i,j)}\right|$$

$$v_{\text{err}} = \frac{1}{NM}\sum_{i=1}^{N}\sum_{j=1}^{M}\left|v_{\text{com}(i,j)} - v_{\text{ori}(i,j)}\right|$$

where NM is equal to the number of velocity vectors of the carrier flow for each image, u_{ori}, v_{ori}, u_{com}, v_{com} are, respectively, the components of velocity along x and y obtained from the original single-phase acquisitions and the same components computed after the discrimination step. In order not to bias the results including velocity vectors lying in the fluid region outside the jet, in our analysis, we leave out the vectors lying in positions where the mean velocity is lower than $0.005U_0$. According to this, roughly 2,200 vectors were used for each one of the processed images leading to an overall vectors number of 352,000 for the carrier phase.

In Figs. 7 and 8, u_{err} and v_{err} are plotted versus T_{int}. The results obtained using the original images are plotted together with those obtained from modified images where brightness and contrast were enhanced or decreased. This is done in order to get results as much as possible independent of the image quality. The results show that as T_{int} increases the displacement errors decrease, reaching an optimal value in the range [$T_{\text{int}} = 60$–100] almost independent on image quality for both velocity components. This behavior is simply explained by considering that when T_{int} is low, too many particles are removed from images, thus resulting in several empty areas which decay the PIV effectiveness. The other way round, high threshold values leave too many particles in the images, leading to poor performance.

Figure 7 shows that with an optimal choice of T_{int}, the displacement error can be reduced to nearly 0.03 pixels (compared to 0.015 pixels in Kiger and Pan 2000) which corresponds to maximum 3 % error with respect to mean

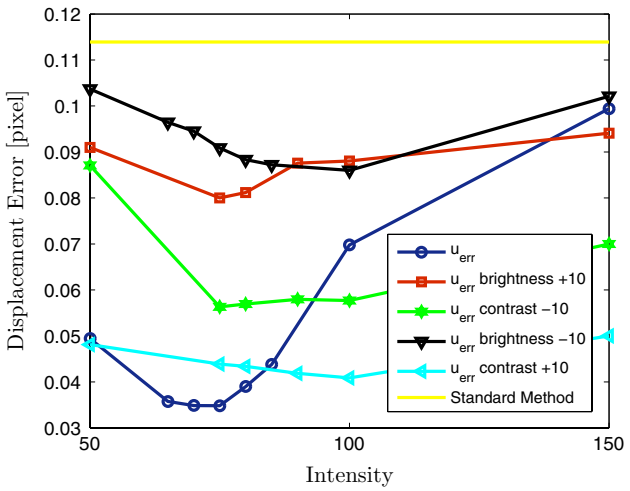

Fig. 7 Longitudinal velocity displacement error induced by phase discrimination on PIV calculations versus intensity value of T_{int}. Data from artificial multiphase images. Comparison among modified images

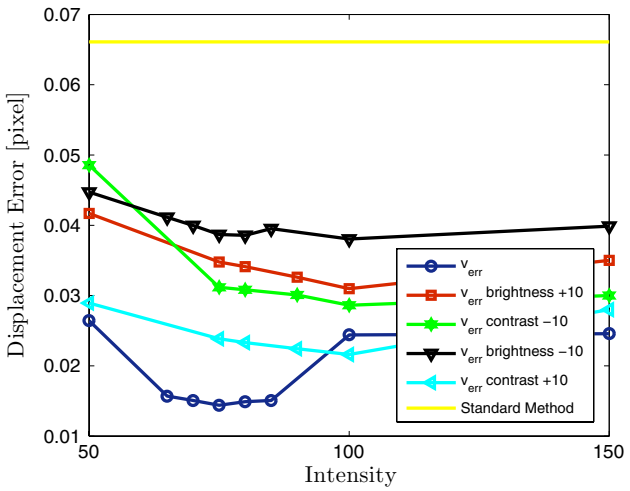

Fig. 8 Transverse velocity displacement error induced by phase discrimination on PIV calculations versus intensity value of T_{int}. Data from artificial multiphase images. Comparison among modified images

displacement. This uncertainty can be considered as the error due to phase discrimination. PDFs of u_{err} and v_{err} show that error due to discrimination is randomly distributed and correlation with particles velocity, obtained by interpolation of u_{err} and v_{err} in particles locations, confirms that the discrimination algorithm does not introduce a bias in the fluid velocity results. In Figs. 7 and 8, the results from phase discrimination using a standard method are also presented. The standard baseline method is implemented via an object recognition algorithm followed by a fixed value threshold on object size (Haralick and Shapiro 1992).

The results presented in the figures clearly show that the phase discrimination method presented in this paper achieves satisfactory performances even in case of poor intensity or contrast.

Results with respect to optimal T_{int} for dispersed phase identification are shown in Fig. 9 where the rates of correct and false detection are reported. Data show that with T_{int} lying within the range [60–100], the rate of detection of fibers is on average approximately 90 %, whereas the rate of false detection is nearly 5 %.

It is now possible to compute again the probability ratio $Pf(i)/Ps(i)$ for such artificial images as described in previous section. Results are presented in Fig. 5 (artificial) in comparison with data obtained from actual multiphase images. The trend of the ratio of the artificial images resembles the one recovered experimentally, and most remarkably, the range of optimal T_{int} derived in Figs. 5 and 8 corresponds to the values just before the plateau, i.e., $T_{\text{int}} \sim 60$–100. Since the discrimination algorithm described so far relies upon the choice of a threshold T_{int}, the sensitivity of the fluid velocity measurements to T_{int} variations should be assessed. To this aim, the evaluation of fluid velocity measurements should include the discussion on phase discrimination algorithm robustness to threshold variations. This will be provided in Sect. 4.2.

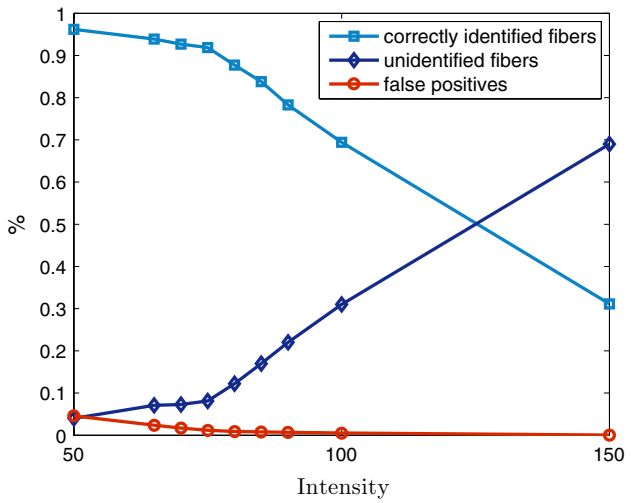

Fig. 9 Percentage of detected and undetected fibers (*bright* and *dark blue squares*) and not correctly detected fibers (*red circles*) versus intensity value of T_{int}. Data from artificial multiphase images

4 Results

In this section, results of PIV/PTV velocity measurements on fluid and dispersed phase are presented. The analysis of results starts with the discussion on boundary conditions and comparisons with literature data for the single-phase conditions, to validate the setup, image acquisition and processing.

4.1 Single-phase flow: data validation and comparison

Figure 10 shows the radial profile of mean and *rms* streamwise velocity for the unladen jet, acquired at 0.1 diameters downstream the pipe outlet. Results are compared to the power-law profile $((1 - \frac{2y}{D})^n$ with $n = 6.5)$ and to the pipe jet experimental data from Vouros and Panidis (2013) and Mi et al. (2001) at Reynolds numbers 5,500 and 16,000, respectively. Comparison of mean velocity profile to literature data shows a good resolution of present measurements and an overall agreement with reference data except for a slight departure in the region close to the boundary of

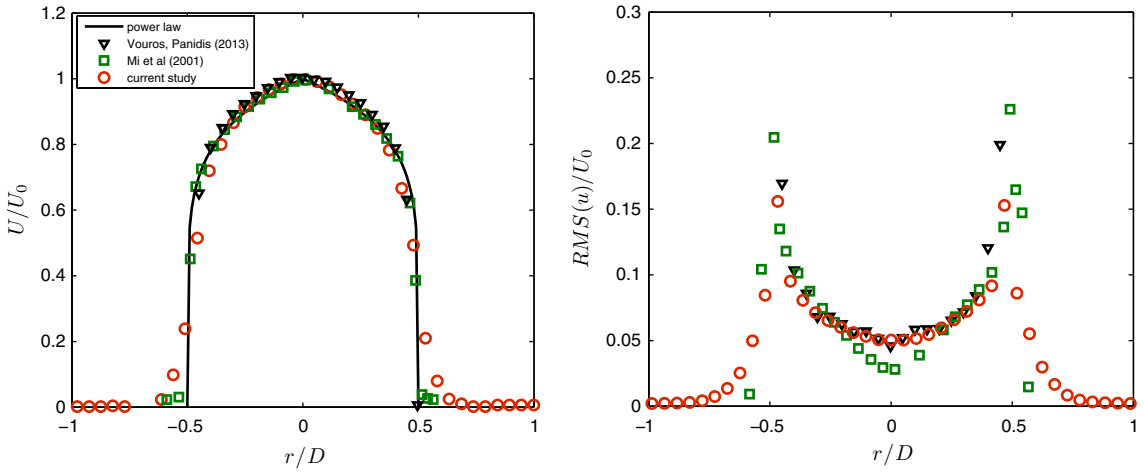

Fig. 10 Inlet velocity profiles (mean on the *left*, rms on the *right*) of streamwise velocity at $x/D = 0.1$ for single-phase jet. The empirical power-law with $n = 6.5$ is used for comparison (Mi et al. 2001) along with data from Mi et al. (2001) and Vouros and Panidis (2013)

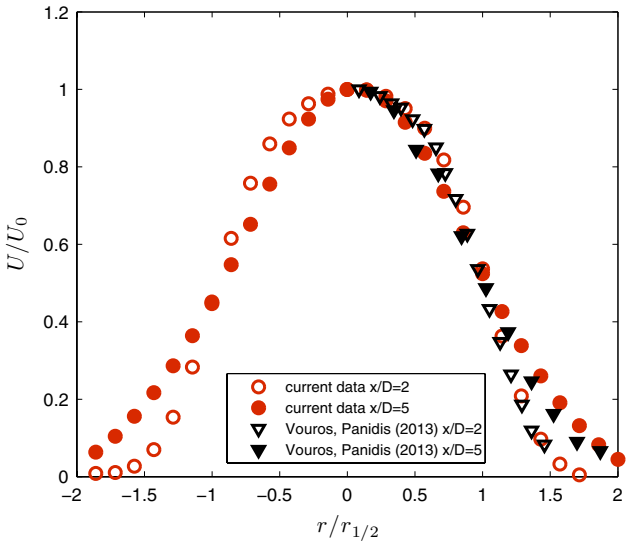

Fig. 11 Mean streamwise velocity at $x/D = 2$ and $x/D = 5$ for single-phase jet compared to data from Vouros and Panidis (2013)

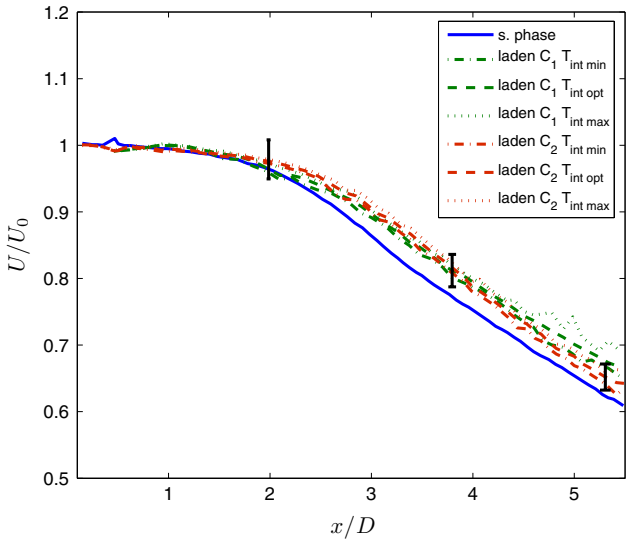

Fig. 12 Streamwise mean velocity of the fluid for single-phase and fiber-laden cases along the jet axis at the centerline. Results displayed for different values of phase discrimination threshold. *Error bar* represents the uncertainty induced by phase discrimination

the jet, i.e., $|y/D| = 0.5$. This is due to the averaging process inherently introduced by PIV computation on a finite size interrogation window. Effects of PIV window size on velocity and velocity gradients measurements in a similar setup are discussed by Lacagnina and Romano (2015). The choice made in this paper follows the suggestions given therein to attain a good spatial resolution. Indeed, comparison to reference data further downstream of the pipe outlet ($x/D = 2$–5) shows how the overlapping is very good at all radial distances as displayed in Fig. 11. Mean velocity profiles compare well in particular to data from Vouros and Panidis (2013), characterized by a Reynolds number close to the present experiment. Overall, results confirm that the flow at the jet inlet is a fully developed turbulent pipe flow.

4.2 Effect of fiber phase on fluid flow statistics

In this section, the effect of fibers on the fluid flow is investigated after phase discrimination. Mean axial velocity decay profiles of the fluid phase are shown in Fig. 12 for the single-phase jet and fiber-laden cases. Data are normalized based on bulk velocity U_0 which is different for single and laden case as opposed to the flow rate, which is kept constant in both conditions. As discussed in Sect. 3.2, it is of interest to assess the robustness of velocity measurements upon the choice of threshold intensity T_{int}. To this aim, fluid velocity data were computed first choosing T_{int} in a so-called optimal way, i.e., in the middle of the identified interval, based on the criteria set out in Sect. 3.2 ($T_{\text{int\_opt}}$, = 75), and then at the lower and higher end of the same interval, respectively, setting the threshold to $T_{\text{int\_opt}}$, $T_{\text{int\_min}} = 50$ and $T_{\text{int\_max}} = 100$. Error bars displayed refer to the maximum uncertainty due to phase discrimination error discussed in Sect. 3.2, calculated at three locations. The results are very similar for different threshold values thus confirming the robustness of phase discrimination procedure. Fiber injection in the flow has a small effect on the mean value for $x/D < 2$. As distance from the pipe outlet grows, a larger velocity for the fluid laden with fibers in comparison with the single phase is noticed. This is in contrast to results found in literature for jet flows laden with spherical particles with a similar d/L ratio (Zoltani and Bicen 1990; Sadr and Klewicki 2005) where single-phase flow and laden flow velocity mean profiles are reported to be substantially identical. Hardalupas et al. (1989) found that the mean flow configuration in spherical particle-laden flows is modified only at mass fractions (20 %) much higher than the present one. Indeed, few works provided results on mean flow modification by fibers. In Krochak et al. (2009), relevant modifications of mean flow structure were reported in the numerical simulation of a tapered channel flow and were attributed to shift in orientation undergone by fibers due to their interaction with the flow. Therefore, discrepancies between sphere-laden and fiber-laden flows, as far as the modification of the mean flow is concerned, should be interpreted in the light of the peculiar dynamics, i.e., strong coupling between rotational and translational motion of fibers in turbulent flows (Krochak et al. 2010).

Radial profiles of mean streamwise velocity, shown in Fig. 13, confirm that the flow with fibers displays an increase in velocity only in the shear layers for $x/D = 1$, whereas for $x/D = 5$, the increase in velocity is mainly confined to the axis and is attenuated along the radial direction.

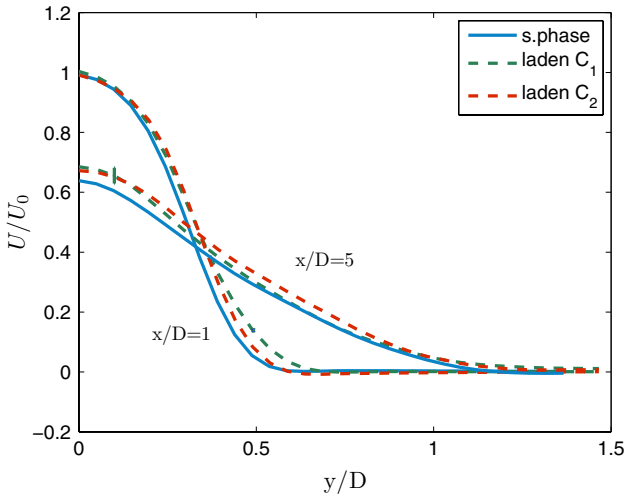

Fig. 13 Radial profile of mean velocity of fluid for single-phase and fiber-laden cases at two downstream positions, $x/D = 1$ and $x/D = 5$. The *error bar* represents the uncertainty induced by phase discrimination

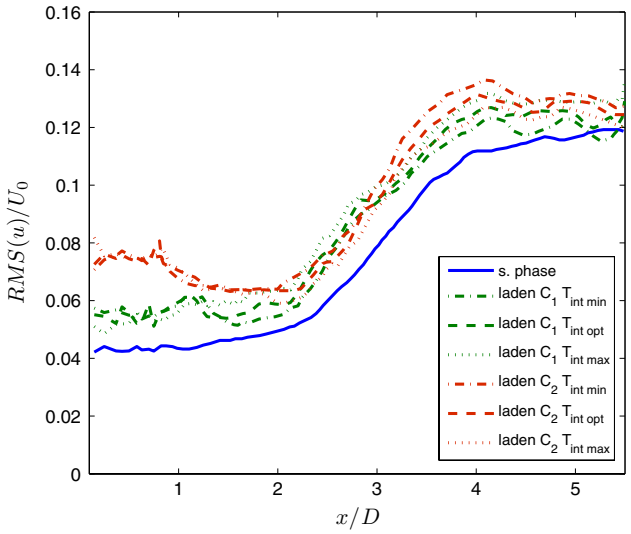

Fig. 14 Root-mean-square value of axial velocity along the axis of the jet at the centerline. Results displayed for different values of phase discrimination threshold

These results confirm that even at such low concentrations, fibers modify the mean flow configuration, supposedly due to elongated particles peculiar dynamics.

As previously reported, Gore and Crowe (1989) proposed a criterion based on the ratio d/L to predict turbulence modulation in particle-laden flows. In the current study, the dispersed phase is represented by rod-like particles and d is set as their largest size, namely the fiber length l. The integral scale L was measured from space correlation functions resulting a value of 10 mm. Consequently, d/L is lower than 0.1, which should lead, accordingly to Gore and Crowe (1989), to turbulence attenuation. The effect of the dispersed phase on turbulence intensity is presented in Fig. 14, where *rms* values of streamwise velocity along the jet axis at the centerline are provided. As in Fig. 12, results stemming from different choices of T_{int} are given for comparison. It appears that the maximum deviation error due to threshold setting is slightly less than 5 %, yielding results almost independent of the specific choice. These results show that the *rms* levels are enhanced at both fiber concentrations by nearly 30 % up to $x/D \approx 4$, i.e., approximately at the end of the jet core region. From there on, the differences with respect to the unladen jet decrease and at the far end of the acquisition window, i.e., $x/D = 5.5$, the relative increment of turbulence intensity is only 5 %. Thus, flow–fibers interactions lead to an increase in turbulence already at the outlet, with only small radial diffusion. PDF of streamwise velocity measured on the jet axis at a sample location $x/D \approx 2$ is provided in Fig. 15 for single-phase and laden cases. It is confirmed that the discrimination step does not introduce a significant amount of spurious velocity measurements that could possibly alter the turbulence

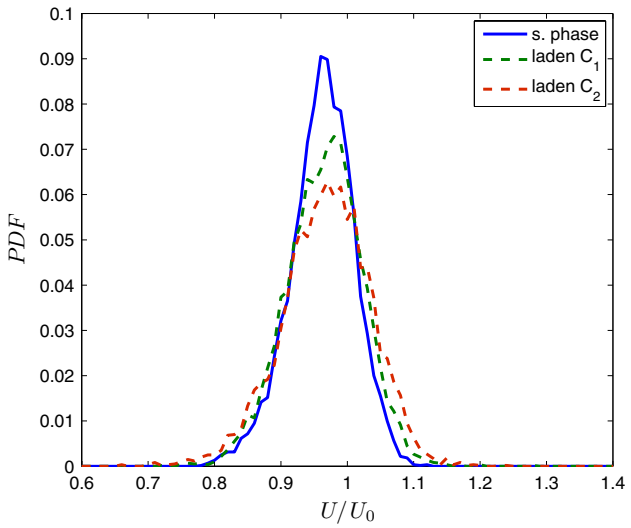

Fig. 15 PDF of instantaneous streamwise velocity along the jet's axis at $x/D = 2$ under single- and multiphase conditions

intensity level, whereas a wider distribution slightly moved toward large velocity values is obtained.

The turbulence increase in the presence of fibers is confirmed at all positions by radial *rms* profiles for both velocity components, reported in Fig. 16. Similarly to Fig. 14, the highest relative increase in turbulence intensity is located in the core region, i.e., around 35 % for the streamwise component at $x/D = 1$ and 8 % at $x/D = 5$, while a small effect of diffusion is observed and with a similar trend for the transverse component.

As for the mean velocity, also *rms* values obtained for the lowest fiber concentration show a similar trend to the

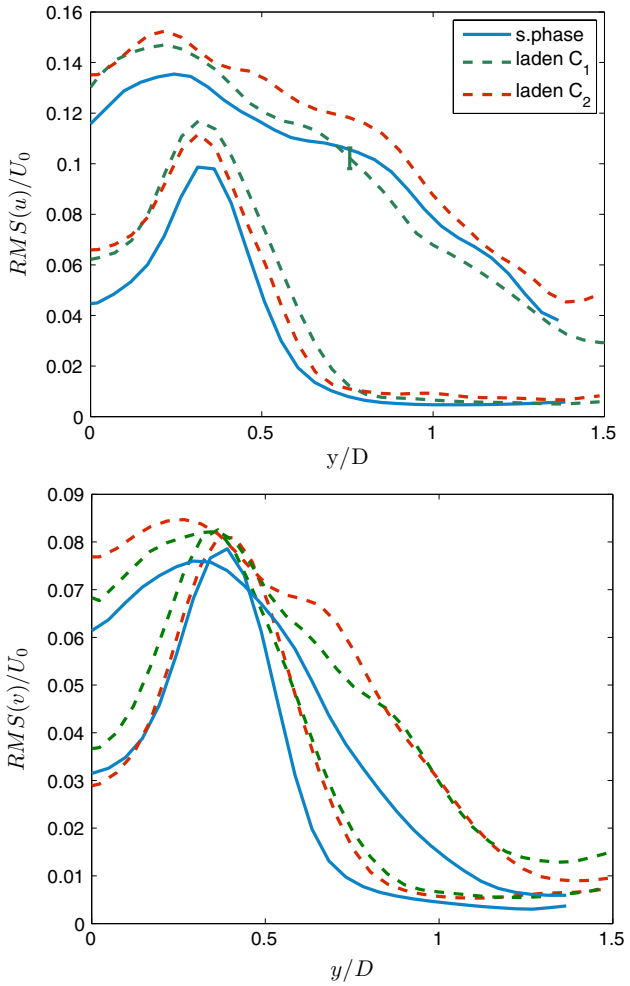

Fig. 16 Root-mean-square of streamwise and radial components of velocity in single-phase and fiber-laden case along radial direction

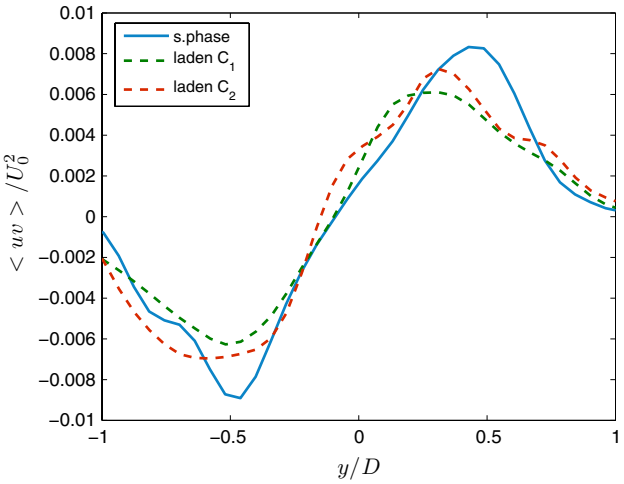

Fig. 17 Radial turbulent shear stress in single-phase and fiber-laden case at $x/D = 3$

highest concentration case when compared to the single-phase jet. Thus, close to the jet outlet, there is a velocity reduction and a turbulence increase which is relevant even at small concentrations. The observed turbulence increments are in clear contrast with the *d/L* Gore and Crowe (1989) criterion. The hydrodynamic drag, which for spherical particles works as a damping factor attenuating fluid turbulence when particles diameter is small relative to large scales, represents at the same time the triggering mechanism of the rotational motion of fibers, as shown by Jeffery (1922). The complex dynamics of fibers stemming from their elongated geometry presumably induces velocity fluctuations in the flow, that have a similar outcome on flow turbulence as larger spheres, enhancing turbulence due to wakes. To the authors knowledge, no experimental work has been so far presented featuring a similar setup, whereas numerical simulations (Yang et al. 2013) recently showed that the modeling of the rotation state of fibers in suspension leads to an increase in turbulence intensity in a pipe jet at low mass fractions (roughly one order of magnitude higher than the current experiment). In order to determine whether the enhanced turbulence in the presence of fibers could be due to the production from the mean motion, Reynolds shear stresses are computed and presented in Fig. 17 for $x/D = 3$.

A decrease is noticed when the flow is laden with fibers, even at the lowest concentration tested. This reveals a reduced turbulence production from the mean flow when fibers are present which is consistent with the reduced axial velocity decay reported in Fig. 12.

4.3 Comparison between the behavior of fluid and particles

Phase discrimination methodologies described in Sect. 3 allow simultaneous calculation of fluid and dispersed phase velocities. In this section, we present velocity results of both phases providing further insight on phase interactions in the present jet flow.

As in all two-phase flows, it is useful to consider the Stokes number to evaluate the particle response to fluid changes. The Stokes number is defined as the ratio of the particle response time τ_p to the characteristic flow timescale τ_f, which is simply computed based on integral length scale L and mean velocity field U. Its importance in the context of particle dispersion in shear flows is discussed in Crowe et al. (1985).

For $St \ll 1$, particles behave as perfect tracers, i.e., they strictly follow the fluid, while for $St \gg 1$, their motion is dominated by inertia, thus not following the fluid.

For $St \approx 1$, the strongest interactions among fluid and dispersed phase will take place with both inertia and dynamic contributions. Calculated Stokes number

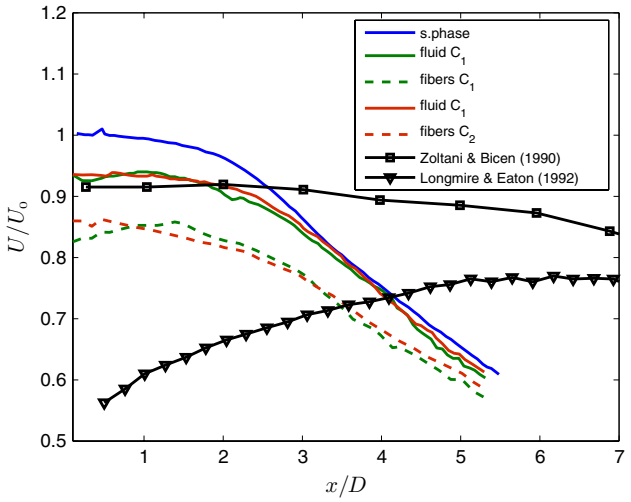

Fig. 18 Mean axial velocity of fluid and fibers along the jet axis at the centerline. Comparison with data from Longmire and Eaton (1992) and Zoltani and Bicen (1990)

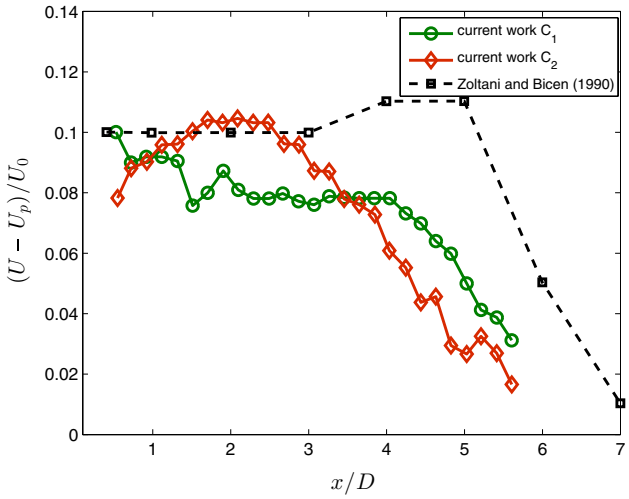

Fig. 19 Fluid–particle mean axial lag velocity among fluid and fibers along the jet axis compared to literature results (Zoltani and Bicen 1990)

for tracer particles is 0.00019, whereas for rod-like particles, *St* is computed according to the formulation of Shapiro and Goldenberg (1993) for the particle response time. This is based on the inverse of the resistance tensor *S* which depends on particle orientation (Marchioli et al. 2010)

$$\tau_p = \frac{2a^2 S}{9\mu} \frac{\ln(k + \sqrt{k^2 - 1})}{\sqrt{k^2 - 1}}$$

where μ is the kinematic viscosity of the fluid and $k = b/a$ represents the fiber aspect ratio, being b and a, respectively, the fiber semimajor and semiminor axes. In this work, the fibers Stokes number varied within the range 0.6–0.7. Relevant interactions among fluid and fibers are then expected, which also allows for explanation of the modifications highlighted in the previous section. Figure 18 reports the mean axial velocity simultaneously measured for carrier and dispersed phase, normalized with respect to the bulk velocity U_0 of the single-phase jet. Clearly, the fibers have an axial velocity which is lower than that of the fluid already from the inlet section. Indeed, a slip velocity is expected for Stokes number close to unity (Zoltani and Bicen 1990; Elghobashi 1994), being the flow fully developed at the pipe outlet, so that dynamical interactions among fluid and fibers are completely established. Fibers data are compared to results from Zoltani and Bicen (1990) who investigated a jet laden with spherical glass particles with similar Stokes number (about 0.3), Reynolds number equal to about 30.000 and mass fraction equal to 1.5 % and from Longmire and Eaton (1992), who focused on a nozzle jet with Reynolds number equal to 20,000.

The mass and volumetric fractions of the former approach the largest concentration of the present experiments. The axial velocity in Zoltani and Bicen (1990) is marked by a delayed decay with respect to fibers data and shows a slower decay rate, whereas data from Longmire and Eaton (1992) feature an increase in axial speed due to the different boundary conditions of the flow. Since the jet investigated in their work originated from a contraction nozzle, it is expected that the particles cannot react instantaneously to the sudden contraction, their inertia accounting for the increase reported along the axial direction. The differences among fibers and fluid decrease when moving downstream along the jet axis.

These results suggest the possibility of momentum and energy transfer occurring between fluid and dispersed phase as they move downstream. It is important to quantify the difference (lag) in mean velocity and how this is balanced by turbulence.

The velocity lag among the two phases is presented in Fig. 19 for the two fiber concentrations. For the smallest concentration, the velocity lag at the jet exit is almost 10 % reducing to about 8 % and then for $x/D > 4$ dropping steadily down to 3 %. For the highest concentration, it is large at the jet outlet (8–10 %) up to $x/D \approx 3$, then reducing to less than 5 % for $x/D > 4$. Fibers at concentration C_1 feature a faster recovery of velocity for $x/D < 2$, while for $x/D > 4$ they display the same behavior as those in the C_2 concentration, with a slight delay in the onset. Data from Zoltani and Bicen (1990) are compared also displaying a lag velocity different from zero already at the jet outlet, being almost constant when moving downstream along the jet axis up to $x/D \approx 5$, where attenuation of differences is observed. The behavior is in rather good agreement with present data for both

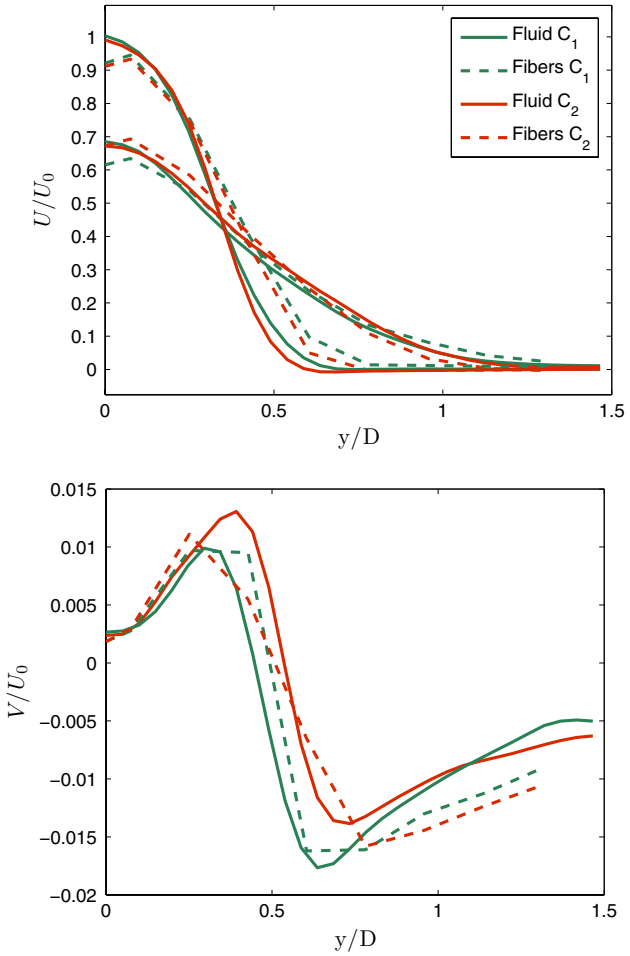

Fig. 20 Radial profiles of mean axial velocity (at the *top*) and mean vertical velocity (at the *bottom*) of fluid and fibers at different downstream positions

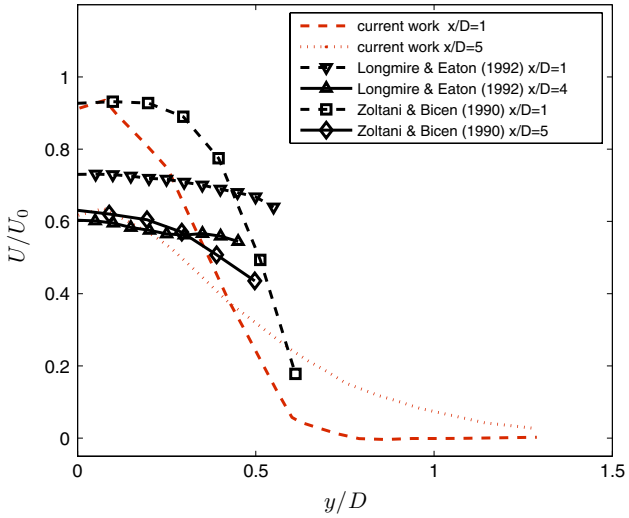

Fig. 21 Radial profiles of fibers mean streamwise velocity at $C = C_2$ compared to data from literature

concentrations, the differences presumably being ascribed to the different solid phase geometry and Reynolds number.

Therefore, there is an initial difference between fluid and fibers already upstream of the pipe outlet and this difference reduces as the jet spreads into the ambient. Fibers retain their velocity for longer distances in comparison with the fluid, so that they should display a reduced interaction with the ambient. This is confirmed in Fig. 20 that depicts the mean streamwise and transverse components of velocity of the fluid and fiber phase in the radial direction. As predicted, in the shear layers, the fibers retain a higher velocity in comparison with the fluid and differences are reduced when moving downstream. Also the vertical velocity, presented in the lower part of the figure, is reduced thus confirming the limited radial spreading in comparison with the fluid due to the effect already described for the fluid alone when laden with a solid phase (see also Fig. 13). Therefore, for the present Stokes numbers, the fiber trajectories are closer to straight lines in comparison with the fluid which displays more complex interactions, especially at the shear layers.

To evaluate the differences in comparison with spherical particles, in Fig. 21, fibers velocity profiles at the highest tested concentration are compared to results from Zoltani and Bicen (1990) and Longmire and Eaton (1992) at similar downstream positions. Fibers show a different radial spreading, especially close to the pipe outlet, in comparison with spherical particles whose profile is flatter. Based on these findings, we can state that, as far as their mean velocity is concerned, although elongated fibers behave similarly to spherical particles, they feature a different interaction with the surrounding flow.

Results presented in the previous section convey a picture where fluid turbulence behavior is markedly different when dispersed particles are represented by fibers rather than spheres. From this perspective, it is interesting to verify whether such a difference could be due to fiber-specific behavior and whether this difference pre-exists already at the jet outlet as suggested by some of previous results.

In Fig. 22, comparison between fibers and flow *rms* of streamwise velocity in the radial direction at $x/D = 0.1$ is given for the highest concentration case along with reference data from Vouros and Panidis (2013). It is observed that also in the fiber-laden case, the flow is completely developed, thus indicating full establishment of dynamical interactions between phases. Fluid and fibers velocity statistics feature differences yet at the pipe outlet. This is not dependent on the specific fiber distribution at the outlet jet. Fiber concentration profile is computed and shown in Fig. 23, where particle concentration n is reported for the highest mass fraction and compared to experimental data by Krochak et al. (2010).

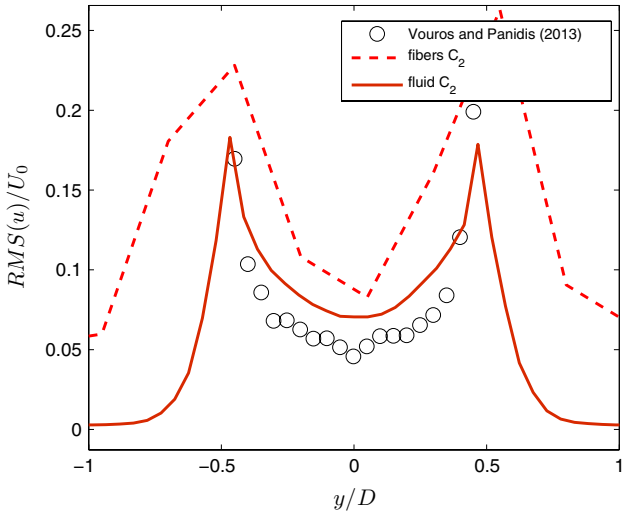

Fig. 22 Turbulence intensity radial profiles at jet outlet ($x/D = 0.1$) of dispersed and fluid phase at $C = C_2$

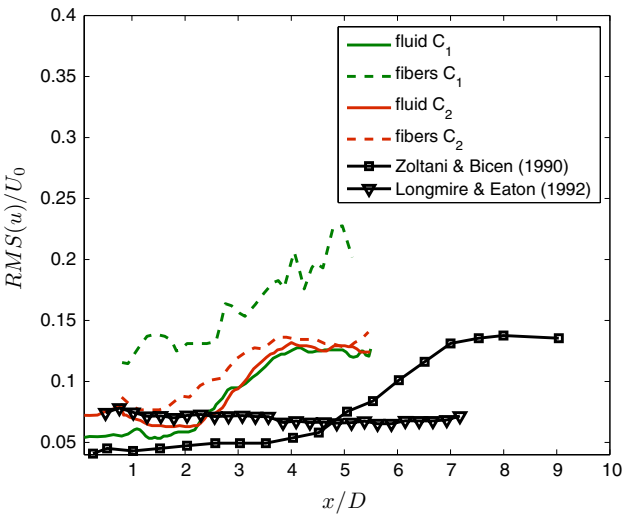

Fig. 24 Profiles along the jet axis of *rms* velocity of fluid and fibers compared to literature data

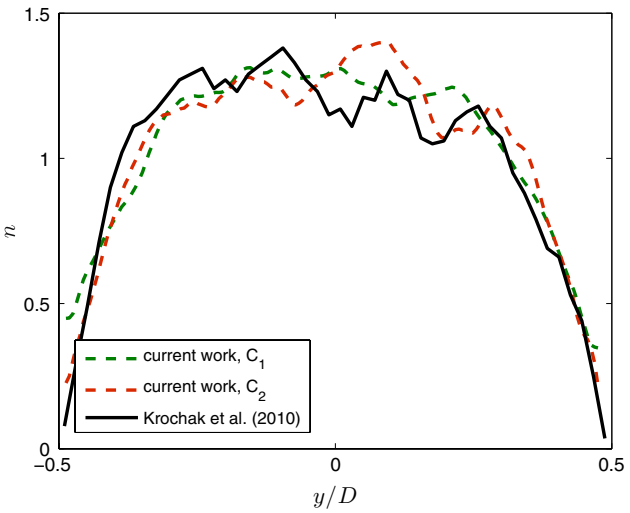

Fig. 23 Fibers concentration profiles at $x/D = 0.1$ compared to channel data from Krochak et al. (2010)

The concentration distribution is renormalized such that the integral across the jet outlet section equals the total number of expected fibers divided by nl^3 according to the following relation

$$\int_0^D n(y)\mathrm{d}y = D$$

The theory of migration of elongated particles predicts that they tend to escape regions of high shear stress while migrating toward low-shear regions (Leighton and Acrivos 1987; Ma and Graham 2005; Krochak et al. 2010), and this is consistent with the given non-uniform particle distribution presented in Fig. 23. In order to establish whether the turbulence levels due to the fibers are similar or not to those attained by spherical particles, axial profiles of streamwise velocity *rms* fluctuations for both phases are computed and provided in Fig. 24. Measured normalized values for the dispersed phase are larger than 20 % (for concentration C_2) and 50 % (concentration C_1) in comparison with those of the fluid phase with the latter results affected by the lower data rate stemming from smaller number of detected fibers. This difference is attenuated when moving downstream, from $x/D = 2.5$–3, where the simultaneous attenuation of the mean velocity lag is also observed, as shown in Figs. 19, 20 and 21. The behavior of the present data well compares with that by Zoltani and Bicen (1990) and Longmire and Eaton (1992) also given in Fig. 24. However, it is clear that fibers are characterized by higher levels of turbulence, supposedly due not only to different boundary conditions, but also to an early onset of turbulence increase compared to spherical particles. The interaction among the two phases is evaluated by means of the fluid–particle velocity correlation coefficient R_{fp}, defined (Sakakibara et al. 1996) as

$$R_{fp} = \frac{\int \left(u_p - U_p\right)\left(u_f - U_f\right)}{RMS\left(u_p\right)RMS\left(u_f\right)}$$

where the subscript p and f refer, respectively, to the fiber and fluid velocity. This coefficient is particularly important to characterize the interactions between phases. In case of high Stokes number, it is directly linked to the turbulent energy extra-dissipation term in the turbulent kinetic energy transport equation (Eaton and Fessler 1994; Sakakibara et al. 1996); nonetheless, it provides valuable information also in regimes where the Stokes number is near unity.

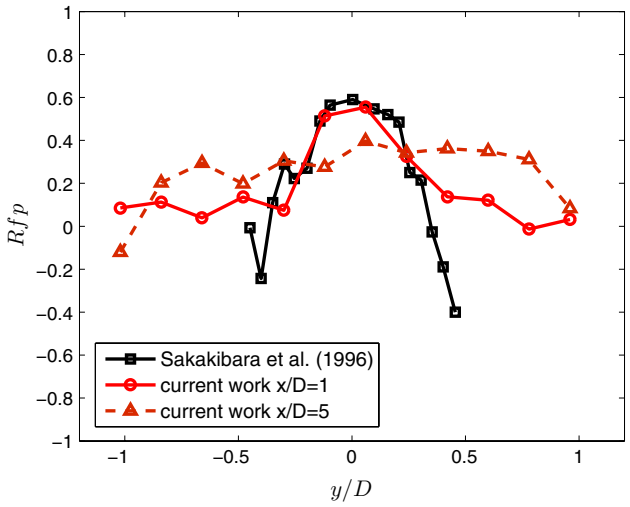

Fig. 25 Fluid–particle streamwise velocity correlation coefficient. $C = C_2$

In Fig. 25, the streamwise velocity fluid–fiber correlation coefficient is shown at $x/D = 1$ and $x/D = 5$ and compared to the results from Sakakibara et al. (1996), obtained in a jet facility loaded with glass spheres ($St = 7.35$).

The instantaneous velocity of the fiber center of mass is multiplied by the instantaneous velocity of the fluid at the same location obtained by trilinear interpolation. It should be pointed out that as shown by Sakakibara et al. (1996), this approach in the calculation of R_{fp} leads to underestimation of the real value. This considered, at $x/D = 1$, fibers feature a similar behavior to spheres, with a less steep decrease near $|y/D| = 0.5$ and a residual correlation for $|y/D| > 0.5$. At $x/D = 5$, the correlation in the core region decreases and has values lower than in the shear regions, assuming a flatter profile along the radial coordinate. This well compares with data in Fig. 20 where for $x/D = 1$ the average velocity difference between fibers and fluid is higher near $|y/D| = 0.5$ thus leading to lower correlation values. Oppositely, for $x/D = 5$, the average difference is more homogeneous along the radial coordinate as it has been reported for the velocity correlation coefficient. These results confirm the peculiar behavior for fibers which tend to correlate with fluid velocity similarly to small Stokes number particles, while they enhance turbulence as reported for large Stokes number particles. This could be partly expected due to the high aspect ratio of such fibers which causes them to be seen by the flow in a way highly dependent on orientation state.

5 Conclusions

An experimental investigation of fluid–particle interactions in a turbulent circular pipe jet laden with rod-like particles at two mass fractions is presented. The Stokes number of the present experimental conditions is around unity, so that complex inertial effects and dynamical interactions are expected.

To investigate in detail such phenomena, an operative and robust phase discrimination method is presented and validated, which is based on extension of the intensity-based algorithm developed by Kiger and Pan (2000). Criteria for optimal intensity threshold choice and reliable estimate of PIV measurement uncertainties are provided along with an extended discussion on applicability and robustness of the proposed method.

Results show that fiber injection has a relevant effect on the mean velocity field as opposed to spherical particles at similar mass loadings, supposedly due to fiber peculiar dynamics. A lag velocity around 10 % has been measured at the jet outlet even at low mass fraction. This difference reduces when moving downstream and laterally.

Turbulence levels in the presence of fibers are from 20 % to 50 % larger than for the unladen jet, and also, this difference is attenuated downstream and moving radially. Results on turbulence intensity are in contrast to turbulence reduction effect observed in flows laden with spheres of comparable d/L ratio, supposedly due to the wakes induced in the flow by the rotational–translational motion of fibers. Fluid–particles correlation data show that fibers correlate in a fashion similar to small Stokes number spherical particles. Detailed study on fibers revealing the nature of fibers–flow interactions and also the dependence on geometrical and dynamical parameters is required in the next future.

References

Balachandar S, Eaton JK (2010) Turbulent dispersed multiphase flow. Annu Rev Fluid Mech 42:111–133

Bröder D, Sommerfeld M (2007) Planar shadow image velocimetry for the analysis of the hydrodynamics in bubbly flows. Meas Sci Technol 18:2513–2528

Capone A, Soldati A, Romano GP (2013) Mixing and entrainment in the near field of turbulent round jets. Exp Fluids 54:1434

Cater JE, Soria J (2002) The evolution of round zero-net-mass-flux jets. J Fluid Mech 472:167–200

Cheng Y, Pothos S, Diez FJ (2010) Phase discrimination method for simultaneous two-phase separation in time-resolved stereo PIV measurements. Exp Fluids 49:1375–1391

Crowe CT, Gore RA, Troutt TR (1985) Particle dispersion by coherent structures in a free shear flow. Part Sci Technol J 3:149–158

Dearing S, Campolo M, Capone A, Soldati A (2013) Phase discrimination and object fitting to measure fibers distribution and orientation in turbulent pipe flows. Exp Fluids 54:1419

Eaton JK, Fessler JR (1994) Preferential concentration of particles by turbulence. Int J Multiph Flow 20:169–209

Elghobashi L (1994) On predicting particle-laden turbulent flows. Appl Sci Res 52(4):309–329

Falchi M, Romano GP (2009) Evaluation of the performance of high-speed PIV compared to standard PIV in a turbulent jet. Exp Fluids 47:509–526

Fleckhaus D, Hishida K, Maeda M (1987) Effect of laden solid particles on the turbulence flow structure of a round free jet. Exp Fluids 5:323–333

Gore RA, Crowe CT (1989) Effect of particle size on modulating turbulent intensity. Int J Multiph Flow 15:279–285

Haralick RM, Shapiro LG (1992) Computer and robot vision, vol I. Addison-Wesley, Reading, pp 28–48

Hardalupas Y, Taylor AMKP, Whitelaw JH (1989) Velocity and particle-flux characteristics of turbulent particle-laden jets. Proc R Soc Lond Ser A 426:31–78

Jeffery GB (1922) The motion of ellipsoidal particles immersed in a viscous fluid. Proc R Soc Lond Ser A 102:161–179

Khalitov DA, Longmire EK (2002) Simultaneous two phase PIV by two parameter discrimination. Exp Fluids 32:252–268

Kiger KT, Pan C (2000) PIV technique for the simultaneous measurement of dilute two-phase flows. J Fluid Eng T ASME 122:811–817

Krochak P, Olson J, Martinez D (2008) The orientation of semidilute rigid fiber suspensions in a linearly contracting channel flow. Phys Fluids 20:073303

Krochak P, Olson J, Martinez D (2009) Fiber suspension flow in a tapered channel: the effect of flow/fiber coupling. Int J Multiph Flow 35:676–688

Krochak P, Olson J, Martinez D (2010) Near-wall estimates of the concentration and orientation distribution of a semi-dilute rigid fibre suspension in Poiseuille flow. J Fluid Mech 653:431–462

Kussin J, Sommerfeld M (2002) Experimental studies on particle behaviour and turbulence modification in horizontal channel flow with different wall roughness. Exp Fluids 33:143–159

Lacagnina G, Romano GP (2015) PIV investigations on optical magnification and small-scales in the near-field of an orifice jet. Exp Fluids. doi:10.1007/s00348-014-1872-8

Leighton D, Acrivos A (1987) The shear-induced migration of particles in concentrated suspensions. J Fluid Mech 181:415–439

Lin JZ, Liang XY, Zhang SL (2012) Numerical simulation of fiber orientation distribution in round turbulent jet of fiber suspension. Chem Eng Res Des 6:766–777

Longmire EK, Eaton JK (1992) Structure of a particle-laden round jet. J Fluid Mech 36:217–257

Ma H, Graham MD (2005) Theory of shear induced migration in dilute polymer solutions near solid boundaries. Phys Fluids 17:083103

Marchioli C, Fantoni M, Soldati A (2010) Orientation, distribution and deposition of elongated, inertial fibres in turbulent channel flow. Phys Fluids 22:033301

Mergheni MA, Sautet JC, Godard G, Ticha HB, Nasrallah SB (2009) Experimental investigation of turbulence modulation in particle-laden coaxial jets by phase Doppler anemometry. Exp Therm Fluid Sci 33:517–526

Mi J, Nobes DS, Nathan GJ (2001) Influence of jet exit conditions on the passive scalar field of an axisymmetric free jet. J Fluid Mech 432:91–125

Paris AD, Eaton JK (2001) Turbulence attenuation in a particle-laden channel flow. Report TSD-137, Department of Mechanical Engineering, Stanford University

Parsa S, Guasto J, Kishore K, Ouellette N, Gollub J, Voth G (2011) Rotation and alignment of rods in two dimensional chaotic flow. Phys Fluids 23:043302

Parthasarathy RN, Chan YH (2001) Turbulence modification in dilute small-particle-laden liquid jets. AIAA J 39:535–537

Parthasarathy RN, Faeth GM (1990) Turbulence modulation in homogeneous dilute particle-laden flows. J Fluid Mech 220:485–514

Prevost F, Boree J, Nuglisch HJ, Charnay G (1996) Measurement of fluid/particle correlated motion in the far-field of an axisymmetric jet. Int J Multiph Flow 22:685–701

Sadr R, Klewicki JC (2005) Flow field characteristics in the near field region of particle-laden coaxial jets. Exp Fluids 39:885–894

Sakakibara J, Wicker RB, Eaton JK (1996) Measurements of the particle-fluid velocity correlation and the extra-dissipation in a round jet. Int J Multiph Flow 22:863–881

Scarano F, Riethmuller ML (2000) Advances in iterative multigrid PIV image processing. Exp Fluids 29:S051–S060

Shapiro M, Goldenberg M (1993) Deposition of glass fiber particles from turbulent air flow in a pipe. J Aerosol Sci 24:65–87

Stanislas M, Okamoto K, Kahler CJ, Westerweel J, Scarano F (2008) Main results of the third International PIV challenge. Exp Fluids 45:27–71

Vouros AP, Panidis TH (2013) Turbulent properties of a low Reynolds number, axisymmetric, pipe jet. Exp Ther Fluid Sci 44:42–50

Yang W, Shen S, Ku X (2013) A new model of turbulent fibre suspension and its application in the pipe flow. Can J Chem Eng 91:992–999

Zoltani CK, Bicen AF (1990) Velocity measurements in a turbulent, dilute, two-phase jet. Exp Fluids 9:295–300